Materials Horizons

ROYAL SOCIETY OF CHEMISTRY

COMMUNICATION

View Article Online
View Journal | View Issue

Cite this: *Mater. Horiz.*, 2026, **13**, 5550

Received 23rd January 2026,
Accepted 2nd April 2026

DOI: 10.1039/d6mh00123h

rsc.li/materials-horizons

Geometry-engineered hourglass-shaped cracks enable wide-linearity wearable strain sensors

Sensen Han,[a] Yan Yue,[a] Milad Razbin,[b] Shuying Wu,[b] Wenkai Chang,[c] Shuai He,[c] Qingshi Meng*[a] and Shuhua Peng *[c]

Flexible and stretchable strain sensors have attracted growing interest for applications in health monitoring and human–machine interfaces. Conventional crack-based resistive strain sensors can achieve high sensitivity and large strain ranges by exploiting the opening and closing of randomly distributed microcracks. However, the uncontrolled evolution of these cracks during prolonged use often leads to performance degradation and poor reliability. In this work, we present a novel resistive strain sensor featuring predefined hourglass-shaped cracks that precisely regulate resistance variations through controlled crack opening and closure under stretching and release. A serpentine array of hourglass-shaped cracks is laser-cut into a 3D-printed conductive TPU film, after which the crack gaps are closed by releasing a pre-stretched elastomer substrate. Through geometric design, crack contact and evolution are precisely controlled, enabling the cracks to open stably and symmetrically under tensile strain, thereby producing predictable and linear resistance changes. This design enables high sensitivity over a broad linear operating range. The sensor also exhibits excellent recoverability after overstretching well beyond its working window and shows negligible resistance variation under bending, highlighting its robustness for wearable applications. To demonstrate its practical utility, the sensor was integrated into athletes' strength-training tasks, and the acquired signals were analyzed using machine learning algorithms to recognize motion patterns and provide early warnings of over-exercise. These capabilities support real-time load adjustment and fatigue-risk management, underscoring the sensor's strong potential for wearable health monitoring and human–machine interface applications.

New concepts

Conventional crack-based strain sensors rely on random crack initiation and growth, making their electromechanical response inherently unpredictable and prone to drift over repeated use. In contrast, this work introduces a geometry programmed crack mechanics concept, in which hourglass-shaped microcracks are deliberately patterned and mechanically preconditioned to dictate crack opening pathways with high precision. By embedding these hourglass cracks within a conductive architecture, the sensor exhibits symmetrically controlled crack evolution, enabling a great combination of broad linear strain range, high sensitivity, ultralow detection limit, and exceptional mechanical stability, even under overstretching or bending. This deterministic control of crack kinematics represents a fundamental shift from crack exploitation to crack engineering, providing a predictable and repeatable electromechanical response. When integrated with machine-learning analysis, the sensor further enables reliable recognition of complex motion states and early fatigue cues, underscoring its strong potential for next-generation wearable health monitoring and human–machine interaction technologies.

1. Introduction

In recent years, flexible wearable sensing technologies have been widely applied in electronic skin,[1–5] motion detection,[6–9] soft robotics,[10–15] and the Internet of Things[16–21] due to their softness, stretchability, and structural simplicity, and they exhibit substantial potential for human–machine interfaces and health monitoring.[22,23] At present, resistive flexible sensors have attracted considerable attention for long-term monitoring of the human body and nonplanar surfaces owing to their simple and efficient fabrication and straightforward signal readout.[24,25] Most previous studies on flexible sensors have primarily focused on achieving either high sensitivity (gauge factor, GF) or a wide working range. However, high GF typically depends on conduction mechanisms such as crack propagation and tunnelling, which often disrupt conductive pathways, thereby reducing the effective sensing range.[26–28] Conversely, sensors designed for wide strain ranges typically exhibit nonlinear responses and reduced sensitivity.[29,30] Therefore, there is an urgent need to develop flexible strain sensors that maintain high sensitivity while simultaneously offering a broad linear working range.

[a] *College of Aerospace Engineering, Shenyang Aerospace University, Shenyang 110136, China. E-mail: mengqingshi@sau.edu.cn*
[b] *School of Aerospace, Mechanical and Mechatronic Engineering, The University of Sydney, Sydney, NSW 2006, Australia*
[c] *School of Mechanical and Manufacturing Engineering, The University of New South Wales, Sydney, NSW 2052, Australia. E-mail: shuhua.peng@unsw.edu.au*

The development of distinctive conductive architectures has been explored by researchers to improve sensitivity and expand stretchability. Studies have shown that strain-induced microcracks provide an effective means to enhance sensitivity.[31,32] Wang *et al.* developed a layered MXene/AgNW composite strain sensor in which through-thickness microcracks enhance sensitivity (GF = 244) while a percolated microcrack network preserves conductivity, enabling a wide linear sensing range up to 60% strain.[33] Additionally, inspired by spider slit organs, Sun *et al.* exploited the large contrast in conductivity and stretchability between Au and SWCNTs to construct a microcrack-based strain sensor that combines high stretchability with extraordinary sensitivity, achieving a wide monitoring range (100% strain) and ultrahigh gauge factors (GF = 7.1×10^4–3.4×10^6).[34] Although such microcrack-based structures can achieve both high sensitivity and a wide detection range, the resistance variations associated with crack opening and closing often display pronounced nonlinearity, and the stochastic evolution of crack morphology during long-term use can cause performance degradation.

To overcome the limitations associated with random crack formation, recent studies have focused on engineering controllable crack architectures by precisely regulating crack initiation, propagation paths, spacing, and density through strategies such as patterned stress concentration, prestraining, and laser ablation.[35–38] Drawing inspiration from the crack-sensing organs in scorpion legs, Meng *et al.* designed ordered concentric-curved crack architectures, achieving exceptionally high sensitivity (0–0.4% strain, GF = 711.1; 0.4–0.8% strain, GF = 7878.6).[39] However, the linear working range remained too narrow for practical applications despite improved stretchability. In contrast, Guo *et al.* introduced a periodically distributed crack-cell architecture in hydrogels to tailor ionic conduction pathways, which significantly broadened the linear sensing range (0–23% strain, GF = 34; 23–170% strain, GF = 2.5; 170–215% strain, GF = 7.1) at the expense of sensitivity.[40] More recently, Wu *et al.* employed a serpentine crack architecture based on Carbon Fiber Reinforced Plastic (CFRP), enabling a flexible strain sensor with high sensitivity (0–2% strain, GF = 82; 2–3% strain, GF = 1226) and an extended linear range.[41] Nevertheless, further broadening the linear sensing range using a single serpentine architecture remains a key challenge.

Based on a new serpentine structural design, this study proposes and experimentally validates an hourglass-shaped crack architecture that enables a strain sensor with simultaneously high sensitivity, a wide detection range, and excellent linearity. The enhanced performance arises from the controlled opening and closing of hourglass-shaped cracks arranged in a serpentine pattern within the conductive layer. While maintaining a high maximum gauge factor of ~108, the sensor extends the linear working range to ~15.5% strain and achieves a low detection limit of 0.01%. The device also exhibits outstanding mechanical robustness, with only 13.1% peak signal drift after 8000 stretch–release cycles at 6% strain, and stable resistance recovery even after over-stretching. Moreover, its low sensitivity to bending minimizes measurement errors on curved or wrinkled surfaces, meeting the demands of monitoring diverse human activities. Coupled with a machine learning algorithm trained on elbow-joint strain waveforms under stepwise loading, the sensor enables early warning of fatigue-related injuries and supports individualized training programs, demonstrating strong potential for practical applications in training monitoring and safety alert systems.

2. Results and discussion

2.1. Fabrication of strain sensor

A pre-defined, hourglass-shaped crack strain sensor with high sensitivity and a wide linear range was fabricated by combining 3D printing, laser micromachining, and a prestrain-enabled packaging process. The overall fabrication workflow is shown in Fig. 1, and additional details are provided in the Experimental Section. Briefly, a conductive TPU filament was 3D printed into a conductive film with a thickness of 500 μm, which was subsequently densified by hot pressing with a platen vulcanizer to 200 μm. Hourglass-shaped slits featuring wide ends, a narrow waist, and smooth filleted transitions were then patterned by laser cutting. During the cutting process, the aperture width (w) at the two ends of the cracks and the array pitch (p) between the centers of adjacent crack units were controlled to fabricate crack units with different parameter combinations, which were electrically connected *via* serpentine interconnects. After ultrasonic cleaning, the conductive film was transferred onto a pre-stretched elastomeric TPU substrate. Releasing the prestrain subsequently closed the hourglass slits. Finally, copper electrodes were attached to both ends of the film for subsequent electrical and mechanical characterization.

2.2. Structure and working principle of the sensor

The overall architecture of the strain sensor is presented in Fig. 2a, which highlights its multilayer configuration and the placement of the hourglass-shaped crack region within the conductive film. The central layer consists of a conductive TPU film, in which hourglass-shaped, predefined crack patterns are precisely introduced *via* laser micromachining. This conductive film is encapsulated within a symmetric sandwich structure formed by elastic TPU layers on both sides, each uniformly coated with an acrylic pressure-sensitive adhesive (PSA) to ensure stable interfacial bonding. Encapsulation with elastic TPU films provides high interfacial compliance, enabling uniform crack opening and closure under deformation. Additionally, the encapsulation layer shields the crack region from humidity, dust, and mechanical abrasion, thereby significantly improving the environmental stability and long-term mechanical durability of the sensor. Moreover, the soft TPU outer layers conform naturally to human skin and irregular or curved surfaces, enabling reliable sensing in diverse scenarios such as joint movements, facial expressions, and other curved-surface scenarios. When a tensile strain is applied, the crack initiates opening at both enlarged ends of the hourglass geometry and then progressively expands toward the narrow central ''waist'', the Fig. 2b shows the crack opening

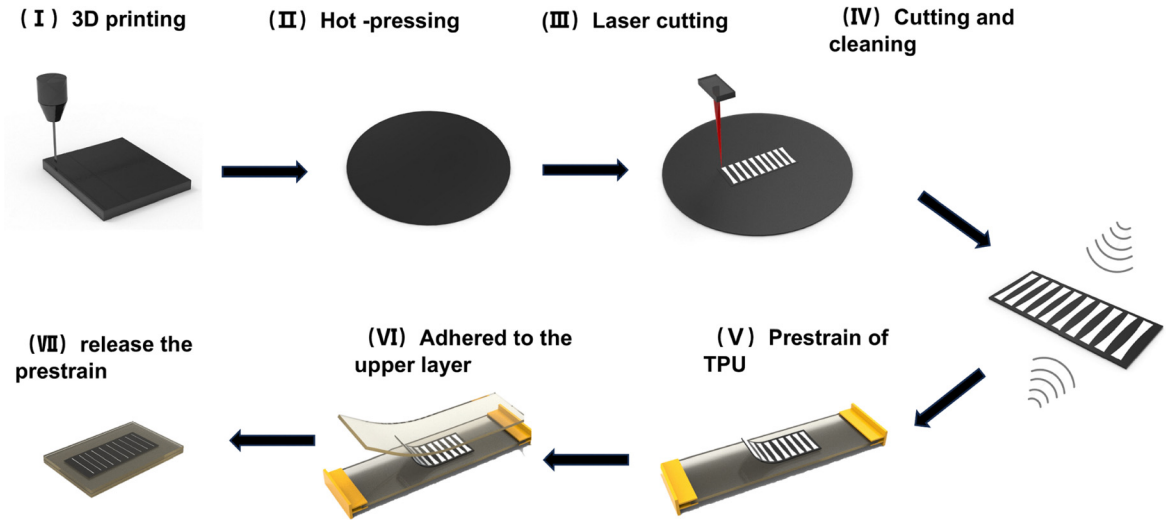

Fig. 1 Schematic of the fabrication process for a flexible strain sensor by transferring a conductive thin film with hourglass-shaped crack patterns onto a pre-stretched TPU encapsulation substrate: (I) 3D printing of conductive TPU film; (II) Hot-pressing for conductive TPU film; (III) Laser cutting of hourglass cracks; (IV) Cutting and ultrasonic cleaning; (V) Prestrain of TPU film; (VI) Transfer and adhesion of conductive TPU film; (VII) Release of prestrain to close cracks.

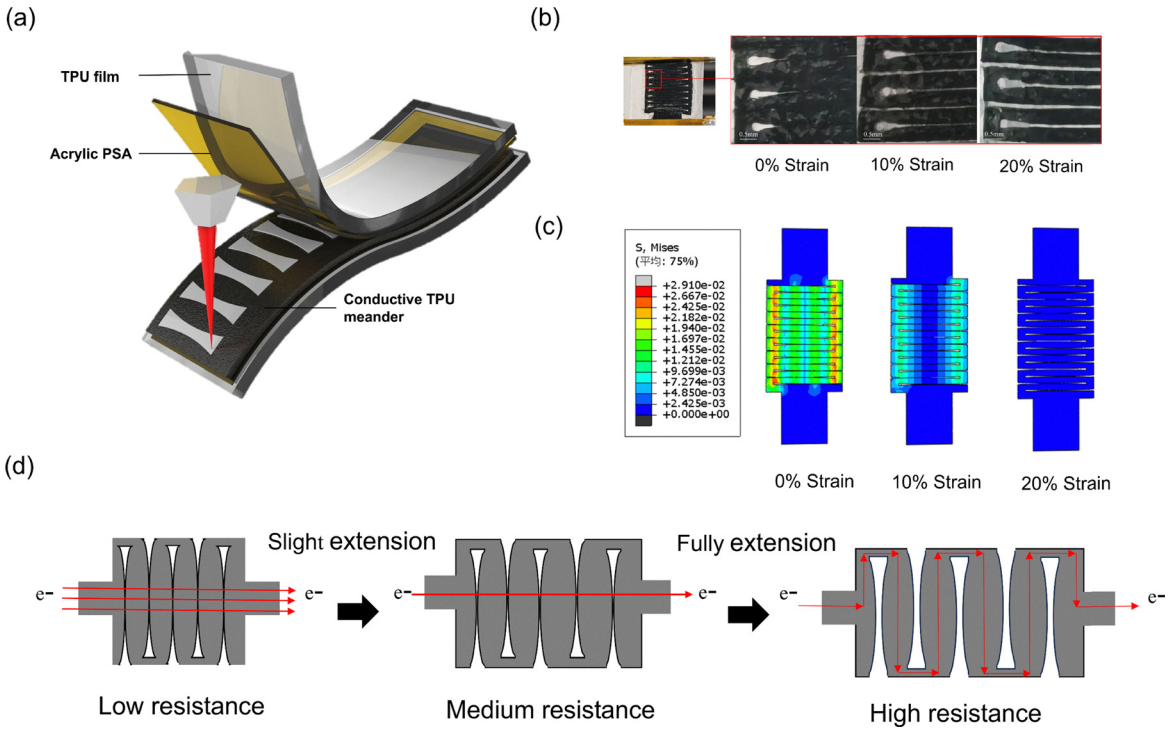

Fig. 2 Structure and working principle of the strain sensor. (a) Multilayer structure of the strain sensor. The TPU encapsulation layer is bonded to the conductive layer with hourglass-shaped cracks using an acrylic adhesive to ensure good elasticity and mechanical performance. (b) When 10% and 20% strain is applied to the sensor, changes in the crack openings can be observed. (c) Finite element simulation of the stretching process with parameters w = 0.35 mm and p = 1 mm, over a strain range of 0–20%. (d) Schematic of the strain sensor's working principle. The opening and closing of laser-cut cracks control the sensor's resistance variation.

conditions under 10% and 20% stress, respectively. This crack-opening behavior was further analyzed using finite element method (FEM). In the initial state, the crack remains fully closed. Under tensile loading, stress is first concentrated at the enlarged ends, causing the crack to open preferentially at these regions and then propagate progressively toward the waist. The simulation results were consistent with the experimentally observed propagation pathway. At a tensile strain of 10%, the stress distribution along the crack edges becomes relatively uniform, signifying the transition into a stable and

controllable propagation stage. When the strain reaches 20%, the crack becomes fully open, corresponding to the upper limit of the designed sensing range (Fig. 2c). The hourglass-shaped cracks combined with serpentine interconnects enable a continuous and highly linear resistance response under strain. Because the enlarged, filleted ends suppress stress concentration and promote smooth crack propagation from the ends toward the waist, the separation between conductive segments increases progressively. This gradual opening, coordinated with the serpentine interconnects that maintain electrical continuity, results in a wide linear sensing range, significantly improving both sensitivity and strain tolerance. Compared to sensors based on straight cracks, this synergistic design provides an expanded linear working range by over 2 times.[42]

The variation in sensor resistance is predominantly determined by the effective current pathways in the conductive thin films, which are modulated by the contact area between hourglass-shaped crack interfaces that bridge neighboring serpentine conductive traces. When the cracks remain fully closed, the conductive traces are directly bridged, resulting in a low-resistance state with minimal interruption to charge transport. Under applied tensile stress, the crack openings initiate at the enlarged ends of the hourglass geometry and progressively propagate toward the narrow central waist. As the effective contact area decreases, the conductive pathways become increasingly constricted, causing the resistance to rise smoothly in synchrony with the geometric evolution of the crack (Fig. 2d). This crack-mediated conduction mechanism provides a predictable and finely tunable resistance response, making it highly effective for strain measurement. During stretching, the hourglass-shaped cracks undergo an approximately linear reduction in effective contact area due to their tailored geometry. This geometric modulation structurally stabilizes the evolution of conductive pathways, suppressing abrupt current fluctuations and ensuring a continuous and smooth resistance transition.

2.3. Sensing performance

To examine the influence of laser-cutting parameters on sensor performance, we varied two key geometric features of the hourglass-shaped cracks, namely the aperture width (w) and the crack array pitch (p), and conducted a series of comparative experiments. Due to the inherent precision limitations of laser micromachining, the end fillet radius cannot be reliably controlled. Therefore, we fixed the minimum waist width at 0.1 mm and indirectly adjusted the fillet radius by varying the aperture width. With the array pitch fixed at 1 mm (p = 1 mm), four w values were selected (w = 0.2 mm, 0.35 mm, 0.5 mm and 0.6 mm), as shown in Fig. 3a. When w = 0.35 mm, the sensor achieves a wider sensing range, as the initially closed cracks resist full opening until the applied strain reaches approximately 16%. Increasing w to 0.6 mm reduces the sensing range to 7.5%, demonstrating that enlarging the end opening significantly compresses the operational strain range. This reduction arises because larger end openings diminish the geometric constraint imposed by the waist, accelerating the loss of effective contact area and causing the resistance to saturate at a much smaller strain. Although a small opening width of w = 0.2 mm produces higher sensitivity (GF = 402.6), the hourglass geometry becomes poorly defined at this scale. This results in a severely narrowed sensing range that cannot satisfy the requirement for wide-range strain detection. Therefore, w = 0.35 mm was selected as the optimal design parameter for subsequent investigations.

With the end opening width fixed at w = 0.35 mm, we varied the crack pitch (p = 1 mm, 1.25 mm, 1.5 mm, and 2 mm) to examine how the spacing between adjacent crack units affects the sensor, as shown in Fig. 3b. The results indicate that increasing p reduces the maximum resistance variation and leads to decline in sensitivity from 108.8 to 43.6. Under identical strain conditions, a smaller pitch yields a higher crack array, this reduces the effective contact area and results in a larger resistance variation, thereby producing a higher sensitivity. In summary, the smaller the parameter p, the greater the resistance change, which is beneficial for improving the sensitivity of the sensor. The size of the parameter w primarily affects the crack closure effect: a larger w influences both the resistance change and the linear range, while a smaller w, although it can provide a larger resistance response, leads to a smaller linear range due to the loss of the constraining effect of the hourglass-shaped crack. Based on the combined influence of both parameters, the cracking sensor achieved optimal performance at w = 0.35 mm and p = 1 mm.

Under identical material compositions and fabrication conditions, we further compared a straight-crack sensor with an hourglass-crack sensor, both designed with the same crack pitch of 1 mm (Fig. 3c). The straight crack structure exhibits a linear electromechanical response only within a limited strain range of 0–9% ($R^2 > 0.99$). In contrast, the hourglass-shaped crack structure significantly broadens this linear regime to 0–15.5% ($R^2 > 0.98$), corresponding to a 72% increase in the usable linear sensing window. This notable extension arises from the more controlled and symmetric crack propagation enabled by the hourglass geometry, which stabilizes the opening and closing behavior under deformation. The expanded linear sensing range is particularly advantageous for applications requiring accurate and reliable strain quantification over larger deformations, such as human motion monitoring, soft robotics, and wearable health diagnostics. The characteristic geometry, featuring wide ends, a narrow waist, and smooth filleted transitions, effectively mitigates stress concentration at the crack tips and smooths the decay of the effective contact area, yielding a more uniform reduction of conductive pathways per unit strain. Consequently, although the sensitivity is reduced, the linear sensing range is significantly extended. We analyzed this comparison process using the Finite Element Method (FEM). Details are provided in the Experimental section.

For the sensor with w = 0.35 mm and p = 1 mm, we tested its resistance response at three different stretching speeds (15 mm s^{-1}, 10 mm s^{-1}, and 5 mm s^{-1}), as shown in Fig. 3d. At 15 mm s^{-1}, the sensor exhibited the highest gauge factor (GF = 120.6), indicating the highest sensitivity, however both

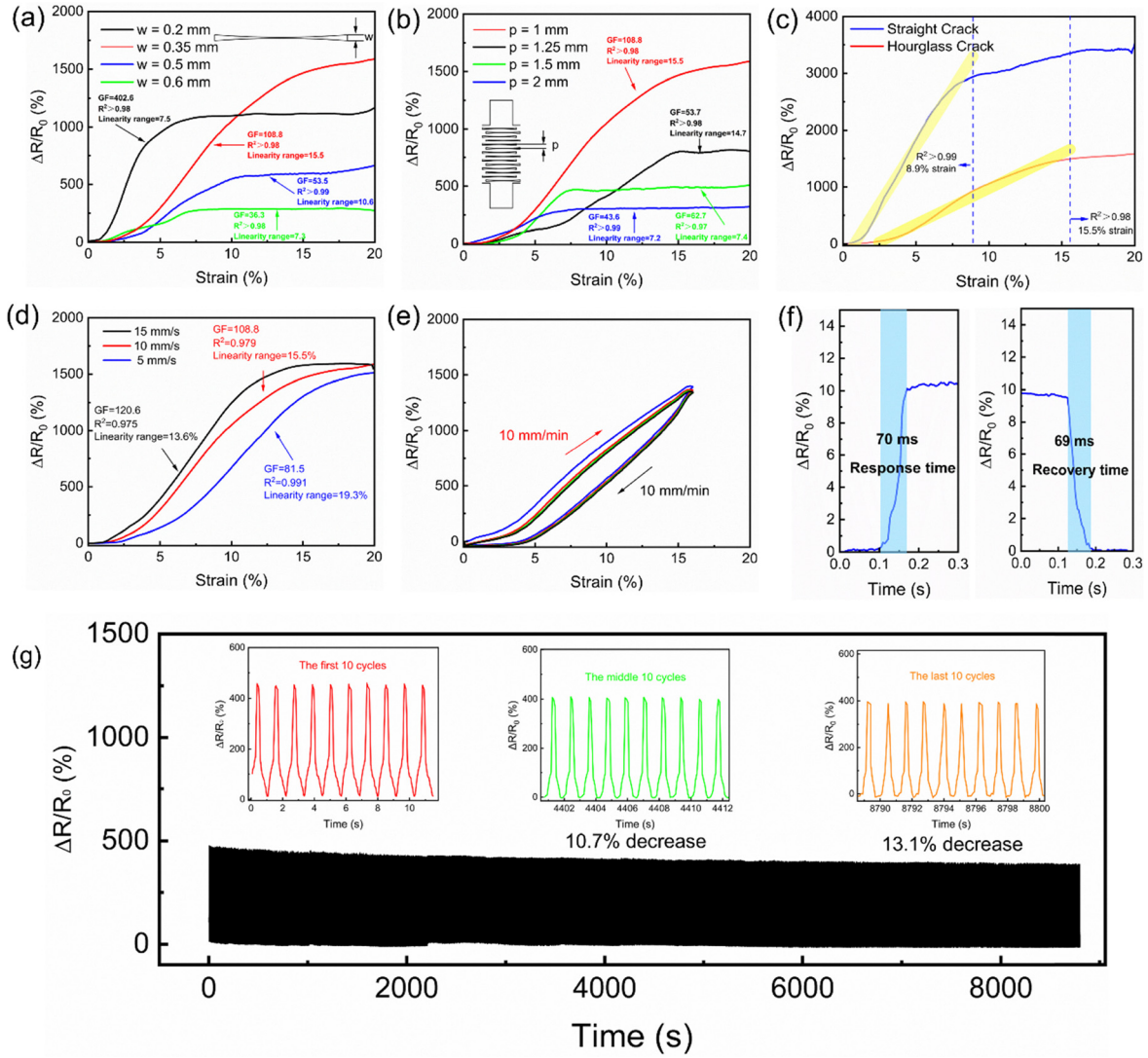

Fig. 3 Effects of hourglass structures under different cutting parameters on sensing performance. (a) Sensor responses for various end-opening sizes of the hourglass (inset: four sensor models with different end-opening sizes, w). (b) Sensor responses for various crack spacings (inset: four sensor models with different crack spacings, p). (c) Comparison of sensor responses between straight and hourglass crack shapes; sensor size and crack-layout parameters are identical (hourglass parameters w = 0.35 mm, p = 1 mm). (d) Resistance response of the sensor at three different stretching speeds. (e) Resistance response at the same stretching rate. (f) Sensor response and recovery times. (g) Sensor response and recovery times. (g) Stability test after 8000 cycles at 6% peak strain; insets show the first 10, middle 10, and last 10 cycles.

the R^2 and the linear range were relatively lower. At 5 mm s^{-1}, the sensor achieved the highest R^2 and linear range, reflecting the best linearity, although its GF was comparatively lower. In contrast, a stretching speed of 10 mm s^{-1} offered a more balanced performance in terms of both sensitivity and linearity, an excellent linear response is achieved: a linear working range reaches 15.5% and a sensitivity of approximately 108.8, demonstrating its capability for wide-range and high-resolution strain detection. The gauge factor (GF), defined as $(\Delta R/R_0)/\Delta\varepsilon$, quantifies the sensitivity, while linearity is assessed using the coefficient of determination R^2. In the linear operating regime, the sensor exhibits R^2 = 0.979, indicating highly predictable resistance–strain behavior. Owing to the viscoelasticity of polymer-based conductive networks, cyclic loading and unloading generate internal friction during molecular chain stretching and relaxation. This energy dissipation leads to non-overlapping loading and unloading curves, giving rise to hysteresis. The sensor exhibits an average hysteresis of 20.1%, which is comparable to the values of strain sensors reported in the literature (Fig. 3e).[42,43] To more clearly illustrate hysteresis effects, we measured response and recovery times: upon triggering, the resistance reaches a steady value within 70 ms. It resistance returned to the initial value within 69 ms after unloading (Fig. 3f). Compared with the response times reported in recent studies on wearable flexible sensors, such rapid response and recovery characteristics make the sensor well suited for real-time monitoring scenarios, including dynamic human-motion detection.[41,44–48] In addition to fast response speed, long-term operational stability and mechanical durability are essential.

Under a 6% strain condition applied over 8000 loading–unloading cycles, the sensor maintains a stable resistance response. The average peak of the middle ten cycles decreases by only 10.7% compared with the first ten cycles and the average peak of the last ten cycles decreases by 13.1% compared with the first ten cycles, The results are comparable to the ones in literatures.[49,50] Demonstrating strong durability and confirming its suitability for long-term or repetitive-motion monitoring (Fig. 3g). To verify the structural stability of the sensor after cyclic loading, we performed optical microscopy observation on the sensor after subjecting to 8000 stretching cycles, as shown in Fig. S3. It can be clearly seen from the image that the pre-designed hourglass-shaped crack structure remains intact with well-defined morphology after cyclic loading, exhibiting no significant degradation or structural collapse of the crack contours. Meanwhile, no obvious random secondary cracks or disordered crack propagation are observed within the imaged region, indicating that crack evolution remains primarily governed by the geometric design. These results demonstrate that the structure possesses good structural stability and fatigue resistance under long-term cyclic loading.

2.4. Strain recognition performance

To evaluate the sensor's ability to resolve different strain levels, we applied a series of cyclic tensile loads with progressively varying peak strains. As shown in Fig. 4a–c, the resulting resistance changes exhibit well-defined amplitude differences, allowing clear and reliable discrimination of the resistance responses corresponding to each applied strain level. Even under small deformations, such as an extremely small strain of 0.01%, the sensor produces a readily distinguishable resistance signal. This demonstrates an exceptionally low detection limit and confirms its suitability for capturing high-precision, small-amplitude inputs. To further verify microstrain recognition, we applied stepwise strain increments of 0.06% with a 5 s dwell after each step and the output resistance closely follows the strain profile (Fig. 4d). The ability to resolve small strain perturbations under large pre-strain conditions is also critical. At a working pre-strain of 5%, the sensor accurately distinguishes an additional 1% cyclic strain (Fig. 4e). Moreover, under a milder condition with 5% pre-strain, the sensor still reliably distinguishes a much smaller cyclic strain of 0.1%, highlighting its ability to detect low-amplitude perturbations superimposedon a static offset (Fig. 4f). Collectively, these results demonstrate excellent resolution and detection capability across different strain regimes, underscoring the sensor's broad potential for strain-sensing applications.

2.5. Mechanical properties

Another notable advantage of the sensor is its exceptional tolerance to overstretching beyond the designated working range. As shown in Fig. 5a, the sensor exhibits a highly linear resistance–strain relationship within the operational strain of approximately 0–20%. When the applied strain exceeds this regime and enters the overstretching region, the sensor still maintains a stable and monotonic resistance response. After holding at the overstretching level and subsequently unloading, the resistance rapidly and reproducibly returns to its initial baseline, demonstrating excellent structural robustness and strong resistance to mechanical overloading. To further evaluate the sensor's recoverability under overstretching deformation,

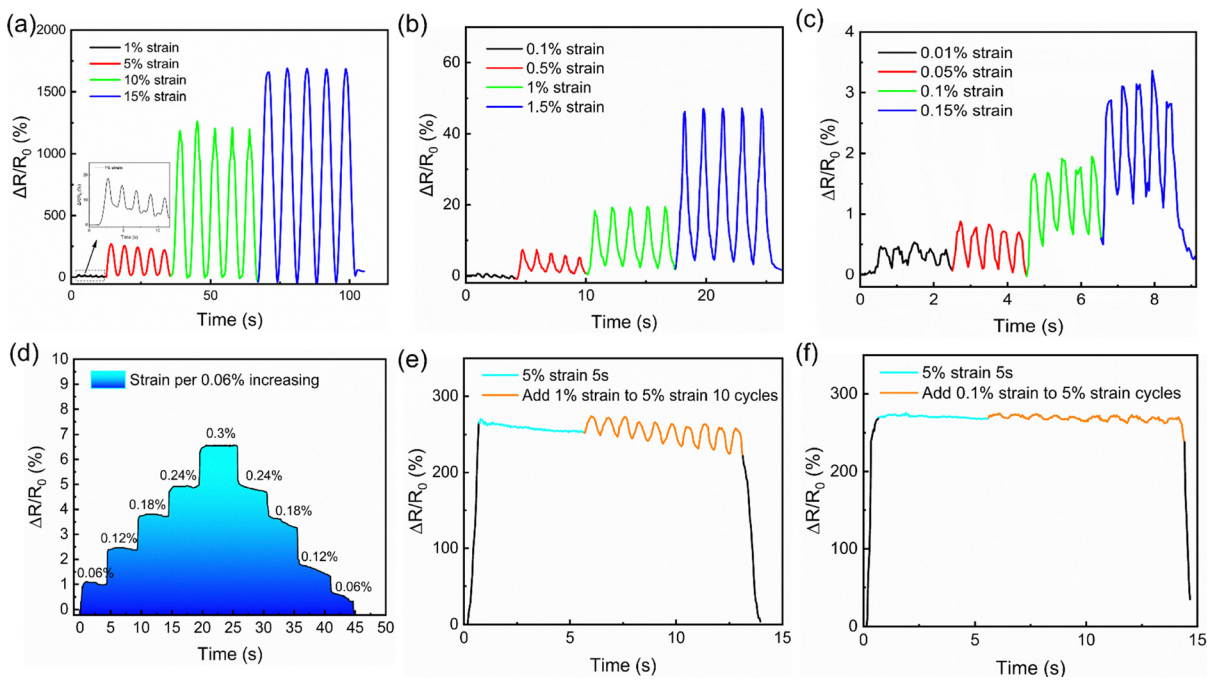

Fig. 4 Strain sensing capability of the strain sensor. (a) Identification of 1–15% tensile strain. (b) Identification of 0.1–0.15% tensile strain. (c) Identification of 0.01–0.015% tensile strain. (d) Response to stepwise tensile strain with 0.06% increments. (e) Identification of a 1% strain superimposed on a 5% applied strain. (f) Identification of a 0.1% strain superimposed on a 5% applied strain.

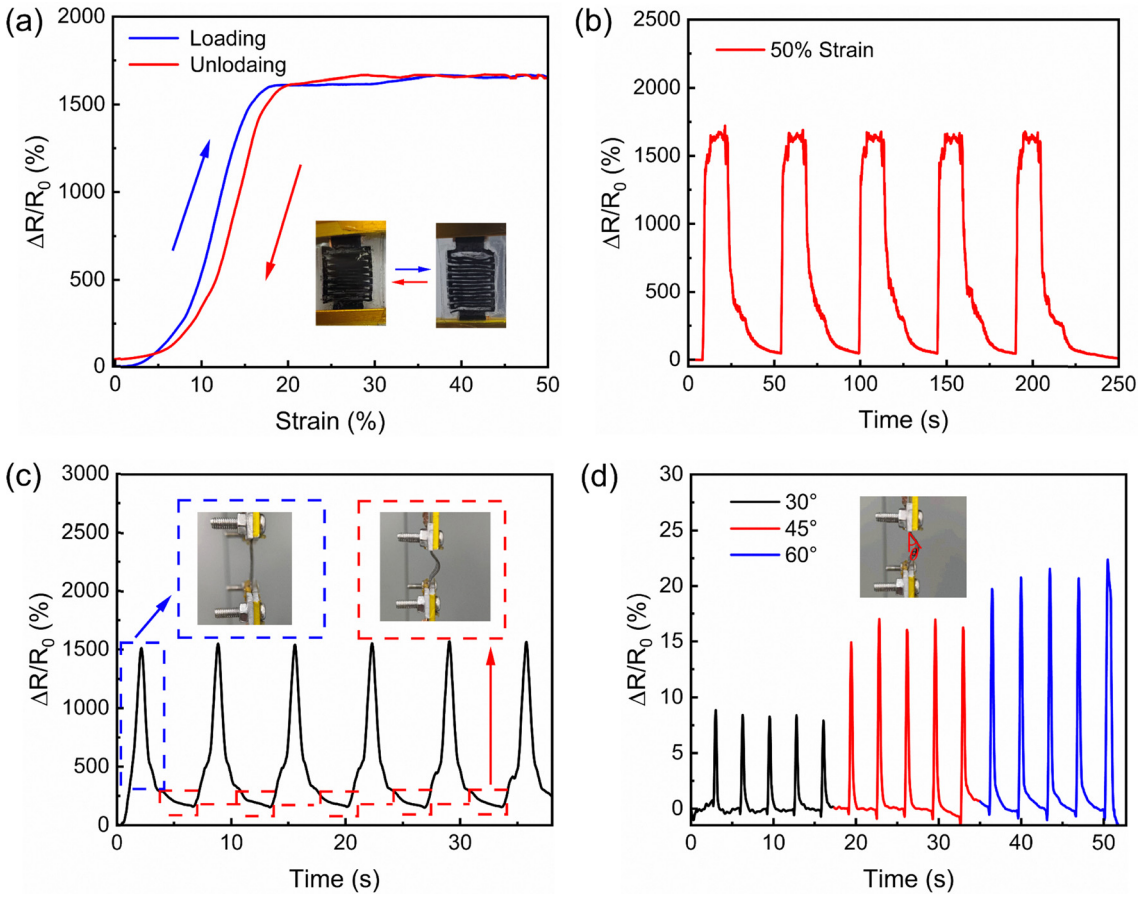

Fig. 5 Overstretch recovery and bending resistance of the sensor. (a) Response of the sensor to overstretching where the strain extends beyond the sensing region. The inset shows the loading (blue) and unloading (red) processes applied in the sensing region. (b) Response of the sensor to repeated overstretch–unload cycles. (c) Response of the sensor to repeated stretch–bend cycles. The inset shows photos of stretching at 20% strain (blue box) and bending at 45° (red box). (d) Response of the sensor at different bending angles.

cyclic loading tests were performed at a high strain level of 50% (Fig. 5b). The peak resistance responses and recovery profiles are highly reproducible, with the baseline resistance fully returning to its original level, demonstrating excellent cyclic stability. No irreversible signal drift is observed when the strain returns from the overstretching state to the working range, indicating that the underlying conductive network is fully recoverable. This behavior is attributed to the unique serpentine architecture, wherein conductive pathways remain continuous despite overstretching-induced separation, and re-close upon unloading to recover sensing performance. Although polymer viscoelasticity inevitably causes a certain degree of hysteresis and stress relaxation during overstretching cycles, no significant cumulative drift was observed. The peak responses remained highly stable across repeated cycles, satisfying the repeatability and reliability requirements typically demanded in health-monitoring applications. In addition to mechanical robustness, environmental stability is equally critical for practical wearable applications.[51–53] To further evaluate the reliability of the sensor under harsh environmental conditions, we conducted accelerated aging tests in a controlled humid and thermal environment (60 °C and 80% relative humidity). As shown in Fig. S4, the sensor maintains a highly linear response and stable sensitivity after both 3 days (5.4% GF decrease) and 7 days (9.1% GF decrease) of exposure, with negligible degradation in performance. Additionally, after thoroughly polishing the encapsulation layer of the sensor with abrasive paper for testing, there was no significant change in the sensor's performance before and after the polishing process (Fig. S5). These results indicate that the encapsulation layer can effectively protect the crack region from external environmental interference, ensuring that the sensor operates stably in real-world working environments.

Bending insensitivity is also critical, as bending-induced deformation is frequently misinterpreted as axial strain in practical measurements using flexible sensors.[54–56] As shown in Fig. 5c, the sensor exhibits a substantial resistance increase of approximately 1500% under 20% tensile strain. After the sensor was unloaded and returned to its original length, applying a 45° bending deformation results in no measurable change in resistance. We further quantified the direct resistance response to bending at different angles in the initial (0% strain) state: at 30°, only an 8% change is observed, which increases to approximately 20% at 60° (Fig. 5d). These bending-induced resistance variations were significantly smaller than

Table 1 Some performance indicators of other sensors

Title	Sensitivity (GF)	First linear strain range (%)	Detection limit (%)	Response time (ms)	Mechanical durability
Strain sensors based on serpentine cracks (ref. 42)	495	8.7	0.01	Not reported	2000 cycles
Flexible conductive hydrogel fibers (ref. 46)	2.49	250	Not reported	120	500 cycles
Strain Sensor Based on Microfiber Coupler (ref. 60)	900	0.45	0.001	0.167	10 000 cycles
Graphene sandwich structure flexible strain sensor (ref. 61)	27.46	30	Not reported	111	3000 cycles
Bioinspired Ultrasensitive Flexible Strain Sensors(ref. 62)	218.13	2	0.1	350	5000 cycles
This work	108.8	15.5	0.01	70	8000 cycles (13.1% drift)

those produced by tensile loading, confirming the sensor's inherently low bending sensitivity. This characteristic is particularly advantageous for minimizing measurement errors when the sensor is applied to complex, curved, or wrinkled surfaces. The interfacial adhesion between the conductive TPU layer and the PSA-based encapsulation was assessed by lap-shear testing. A shear strength of approximately 0.93 MPa was obtained, confirming robust bonding at the interface. This strong adhesion helps maintain structural integrity under repeated bending, contributing to stable electrical performance[57–59] (Fig. S6).

To highlight the advantages of our sensor compared to recent flexible strain sensors, a quantitative comparison is presented in Table 1. By comparing some key parameters of our sensor with those reported previously, this can provide useful insights for the future optimization of flexible strain sensors.

2.6. Monitoring human motion

Benefiting from its excellent strain sensing performance, the sensor shows broad potential for human health monitoring

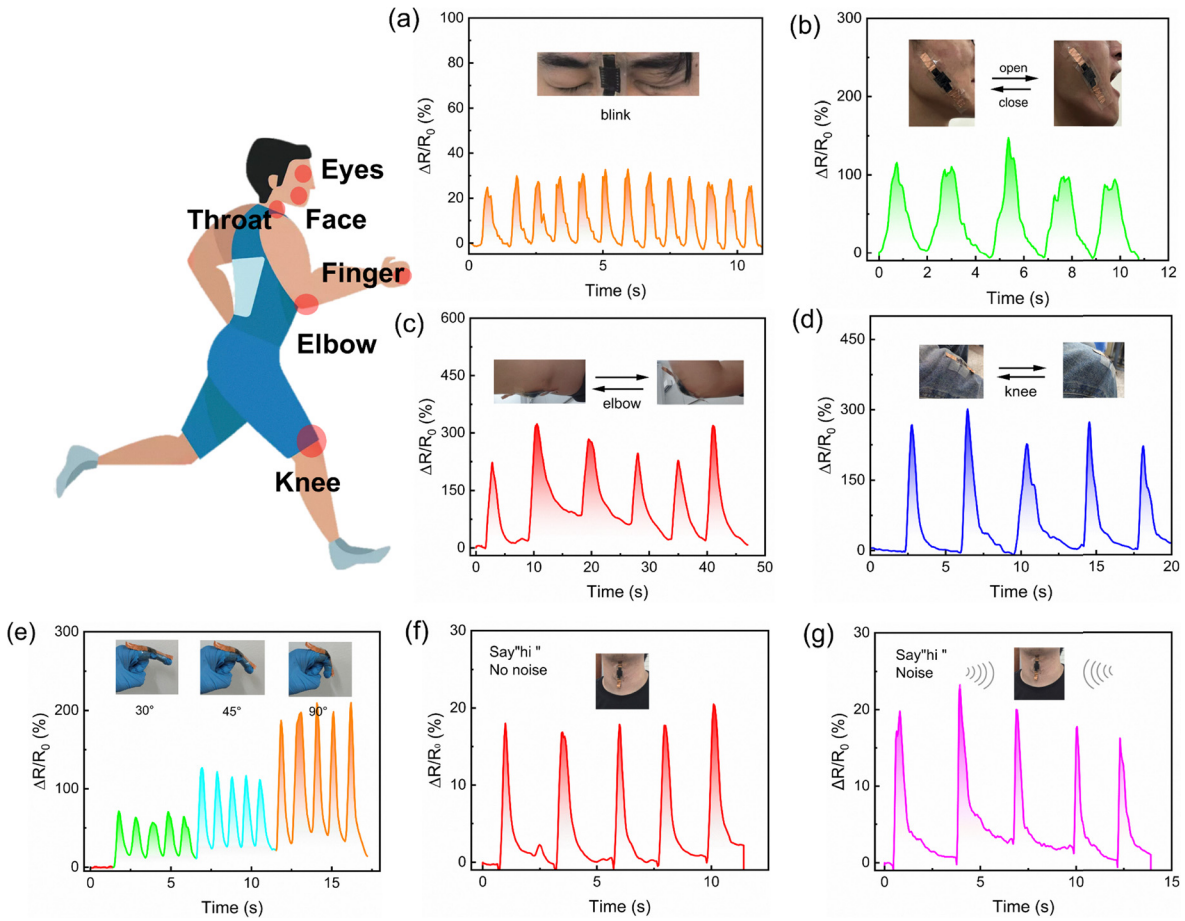

Fig. 6 Applications of the sensor in human body parts and joint bending. (a) Sensor response to blinking. (b) Sensor response to mouth opening and closing. (c) Sensor response to elbow flexion. (d) Sensor response to knee joint bending. (e) Sensor response to finger joint bending at 30°, 45°, and 90°, respectively; the inset shows the finger joint at 0°, 45°, and 90°. (f) Sensor response at the throat to saying "hi" in a quiet environment. (g) Sensor response at the throat to saying "hi" in a noisy environment above the sensor and corresponding response mapping of pressure distribution.

and human–machine interaction (HMI). The sensor enables monitoring of diverse motions when worn at different body sites. Its real-world wearable usability was evaluated by mounting it on the face, joints, and limbs to continuously track micro-facial expressions, joint flexion/extension, and voice activity. For subtle physiological activities within low-strain regimes (<20%), the sensor exploits its high sensitivity and extended linear range to accurately resolve fine motion details. During skin deformation and joint bending, the sensor predominantly experiences bending-induced traction rather than pure tensile strain. Due to its relative insensitivity to bending, the resulting resistance variation remains moderate and avoids saturation, thereby preserving the ability to differentiate between bending amplitudes. At the same time, the sensor maintains good distinguishability and repeatability across varying deformation levels. Consequently, even when the applied strain exceeds the nominal linear range, the sensor can still effectively discriminate motion amplitudes through characteristic waveform features, enabling reliable

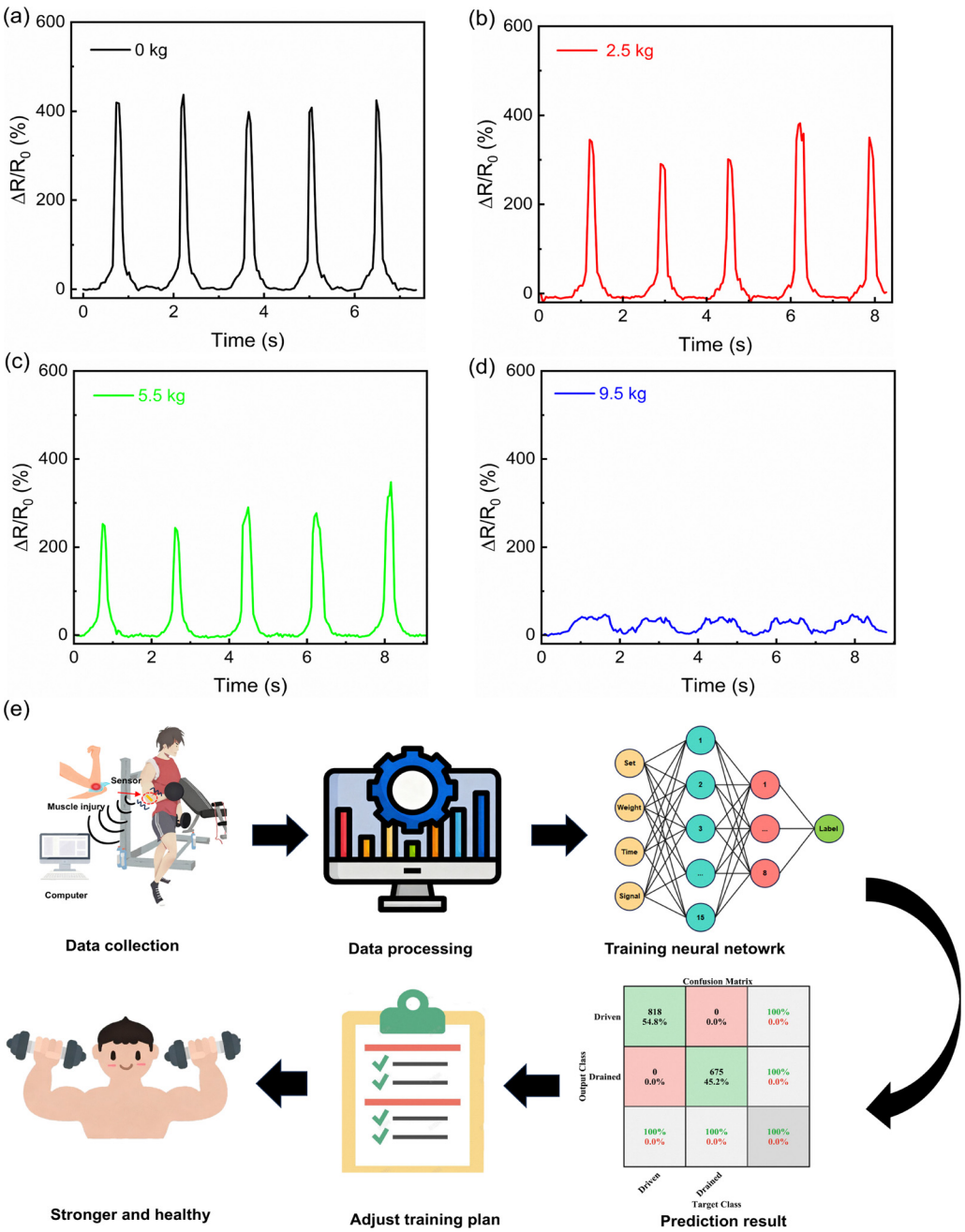

Fig. 7 Integrating sensor output signals with machine learning algorithms for early-warning and planned adjustments in athletes' strength training. (a) Sensor response at a training load of 0 kg. (b) Sensor response at a training load of 2.5 kg. (c) Sensor response at a training load of 5.5 kg. (d) Sensor response at a training load of 9.5 kg. (e) Workflow of the application, with an illustration showing data collection, data processing, neural network training, prediction results, and training plan adjustment.

performance in practical scenarios where skin and joint strains are relatively large. Fig. 6a and b present the monitoring of eye blinking and mouth opening/closing, where each action yields a distinct resistance response, indicating reliable detection of facial-expression changes. On the upper/lower limb joints and fingers, the sensor stably tracked flexion–extension and angle variations. Clear and repeatable resistance signals were observed for elbow (Fig. 6c) and knee (Fig. 6d) movements, and finger bending at 30°, 45°, and 90° was accurately distinguished (Fig. 6e). In addition, when conformally attached to the throat, speaking "hi" produced a pronounced resistance response (Fig. 6f), which remains unaffected in the presence of ambient noise (Fig. 6g). These capabilities underscore the device's strong potential as a flexible electronic skin sensor, enabling applications in rehabilitation assessment, motion capture, and HMI.

Resistance training is a cornerstone for enhancing athletes' maximal strength, explosive power, and sport-specific performance, and its effectiveness depends on the scientific rigor and degree of individualization of the training program. If the program is inappropriately designed (*e.g.*, in intensity or frequency), muscle overuse or strain can readily occur, leading to training interruptions and fluctuations in performance. It emphasizes the importance of wearable sensing technologies for real-time monitoring and individualized training regulation.

To demonstrate the applicability of the developed sensor for human performance monitoring, an artificial intelligence (AI)-based feedforward backpropagation neural network (FBNN) was employed to classify an athlete's training state as either driven (energized) or drained (fatigued). The dataset included four key input features: number of sets, weight or load, time, and sensor output signal, collected from the sensor system during strength exercises (Fig. 7a–d). The neural network architecture consisted of an input layer with four neurons, two hidden layers with 15 and 8 neurons using a hyperbolic tangent sigmoid transfer activation function, and an output layer with a softmax function to predict the two classes (Fig. 7e). The network was trained using the scaled conjugate gradient backpropagation algorithm, with 80% of the data used for training, 5% for validation, and 15% for testing. Label encoding was defined as 0.1 for driven and 0.9 for drained states, allowing the model to interpret physical exertion levels based on variations in the sensor signals. The training minimized cross-entropy loss, achieving over 99% classification accuracy, as confirmed by the confusion matrix. This AI-integrated approach enabled real-time recognition of fatigue states and provided adaptive feedback for adjusting training load, demonstrating the potential of combining intelligent sensing and neural network analysis for personalized strength training management.

3. Conclusions

In this study, we developed a flexible strain sensor featuring hourglass-shaped cracks that simultaneously offers a wide linear sensing range, high sensitivity, an ultra-low detection limit, and mechanical robustness. This is achieved through the design of hourglass-shaped cracks interconnected in a serpentine pattern within the conductive film. To quantify the impact of end-opening width and array density on performance, we conducted a systematic parametric study and identified a geometry that balances high sensitivity with a wide range, achieving a linear sensing range of approximately 15.5%, a sensitivity (GF) of about 108.8, and excellent linearity ($R^2 \geq 0.98$). The sensor also exhibits outstanding resolution across different strain regimes, with a minimum detectable strain as low as 0.01%. Owing to the controllable structural design, the device maintains sensing capability under overstretching well beyond its nominal working range and rapidly recovers to the initial state upon release. Moreover, it displays low bending sensitivity, substantially reducing measurement errors on complex curved surfaces. When conformally attached to body sites such as the eyes, mouth, and various joints, the sensor reliably identifies clear motion signals. To highlight its relevance to health monitoring and HMI, we further integrated the sensor with machine learning and placed it on an athlete's elbow to track fatigue during strength training. Overall, the sensor shows broad application prospects for human health monitoring and HMI, providing high-sensitivity measurements over a wide range together with strong robustness in practical use.

4. Experimental section

4.1. Materials

Thermoplastic polyurethane (TPU) tape was supplied by Kangkejian Biotechnology Co., Ltd (Guangzhou, China). Conductive TPU 3D-printing filament was obtained from Yousu 3D Technology Co., Ltd (Guangzhou, China). The 3M 1181 conductive copper-foil tape was provided by Bazhiteng Electronic Technology Co., Ltd (Suzhou, China). In addition, the conductive silver paste was purchased from Luxianzi Technology Co., Ltd (Shenzhen, China).

4.2. Preparation of sensors

The conductive layer is fabricated using CB/TPU 3D printing filament as the raw material, in which carbon black (CB) is incorporated as the conductive filler within the printing strand, achieving a resistivity of 7 Ω cm. Using fused deposition modeling (FDM) 3D printing technology, the sensor layer precursor film is printed under the temperature settings of 210 °C for the upper bed and 30 °C for the lower bed, with a thickness of 500 μm. The default fast print setting was selected for print speed. The TPU after 3D printing is shown in Fig. S7. The as-printed films were subsequently hot-pressed using a platen vulcanizer to produce densified films with a final thickness of approximately 200 μm, the temperatures of the upper and lower platens were both set to 210 °C. Preset hourglass-shaped cracks arranged in a serpentine pattern were introduced by laser cutting. The laser parameters were: 20% laser power, 30 mm s^{-1} scanning speed, and a nominal processing head width of 100 mm. The toolpath was designed in CAD; in

curved regions, a single trace shuttled between adjacent features to minimize line spacing. Two groups of samples with different designs were prepared: Group 1: fixed slit width w = 0.35 mm; pitch p = 1.0 mm, 1.25 mm, 1.5 mm, and 2.0 mm; total length 43 mm; Group 2: pitch p = 1 mm; slit width w = 0.2 mm, 0.35 mm, 0.5 mm, and 0.6 mm; total length 43 mm. Each layout integrated rectangular contact pads (9 mm × 10 mm) for electrical connection *via* copper foil. After ultrasonic cleaning and drying, the patterned film was transferred onto a TPU substrate pre-stretched (width 15 mm, thickness 200 μm), fixed with mechanical clamps, and bonded using an acrylic pressure-sensitive adhesive. Before applying the copper foil, a silver conductive paste was coated on the contact pads; another TPU film, pre-stretched in the same manner and coated with adhesive, was then laminated to complete encapsulation. Upon releasing the pre-stretch, the hourglass cracks closed and the serpentine network became electrically connected. Finally, the sensor was cured at 75 °C to set the silver conductive paste. Regarding Fig. 3c, Finite element analysis (FEA) performed under identical simulation conditions further shows that, at the same applied strain, hourglass cracks exhibit smaller opening displacements and a smoother, more gradual crack-opening process compared with straight cracks. At a strain of 15%, the straight cracks are already fully opened, whereas the hourglass cracks still retain additional opening capacity, indicating a larger operable strain margin (Fig. S1). As shown in Fig. S2, the change in contact area of the two types of closed cracks under strain is presented.

4.3. Characterization

The conductive film was printed using a 3D printer (Raise3D Pro2, Shanghai Fuzhi Information Technology Co., Ltd). Laser cutting was performed with a laser cutter (SF960, Jinan Senfeng Technology Co., Ltd). Hot-press molding was conducted on a platen vulcanizer (YF-8017, Yangzhou Yuanfeng Testing Equipment Co., Ltd). Tensile testing of the samples was carried out on a universal testing machine (SL-018MD, Shenyang Sihongda Technology Co., Ltd). The sensor resistance was measured using an LCR digital bridge (TH2829, Changzhou Tonghui Electronics Co., Ltd). A humidity chamber with temperature control (MW3030, Guangzhou Gaohua Instrument Equipment Co., Ltd) was employed for the humidity testing of strain sensors under different temperature conditions.

Conflicts of interest

The authors declare no conflict of interest.

Data availability

The data supporting the findings of this study are available within the article and its supplementary information (SI). Additional datasets or raw experimental data are available from the corresponding author upon reasonable request. Supplementary information: FEM analysis of straight cracks and hourglass-shaped cracks strain sensors; Microscopic image of the sensor after 8000 cycles; the impact of humid and thermal environment on sensor performance; the interfacial adhesion between the conductive TPU layer and the PSA-based encapsulation was assessed by lap-shear testing; image of 3D printing conductive films with thickness of 500 μm before cutting. See DOI: https://doi.org/10.1039/d6mh00123h.

Acknowledgements

This work was financially supported by the Fundamental Research Funds for The Universities of Liaoning province (LJ212510143025) and the Liaoning Province Science and Technology Joint Program (Key R&D Program Project) (2025JH2/101800288).

References

1 Y. He, X. Xu, S. Xiao, J. Wu, P. Zhou, L. Chen and H. Liu, *ACS Sens.*, 2024, **9**(5), 2275–2293.
2 Q. Tang, M. Zou, L. Chang and W. Guo, *Chem. Eng. J.*, 2022, **430**(Part 4), 132152.
3 W. Yang, W. Ding, L. Menglong, Y. Jun and L. Mao, *J. Phys. D: Appl. Phys.*, 2022, **55**, 094001.
4 S. Han, P. Wang, Y. Zhou, Q. Meng, M. Aakyiir and J. Ma, *Compos. Sci. Technol.*, 2022, **230**, 109451.
5 L. Veeramuthu, C.-J. Cho, M. Venkatesan, H.-Y. Hsu, B.-X. Zhuo, L.-J. Kau, M.-A. Chung, W.-Y. Lee and C.-C. Kuo, *Nano Energy*, 2022, **101**, 107592.
6 X. Guo, Y. Niu, Z. Yin, D. Wang, L. Liu, Y. Tang, X. Li, Y. Zhang, Y. Li, T. Zhang, X. Zhu, Y. Xu, Z. Zhang, S. Ding, D. Wang, B. Yang, Z. Mai, W. Hong, W. Xu, Q. Hong, Y. Zhao, F. Yan, M. Wang and G. Xing, *Adv. Mater. Technol.*, 2024, **9**, 2400701.
7 M. Wang, L. Hou, Y. Xiao, R. Liu, H. Lu, N. Mukhurov, Z. Siqi, C. Chuantong and H. Kuan, *Langmuir*, 2023, **39**(45), 15911–15919.
8 H. Zhou, S. Li, H. Liu, B. Zheng, X. Jin, A. Ma and W. Chen, *Macromol. Mater. Eng.*, 2019, **305**, 1900621.
9 Y. He, Y. Ming, W. Li, Y. Li, M. Wu, J. Song, X. Li and H. Liu, *Sensors*, 2018, **18**, 1338.
10 G. Gerboni, A. Diodato, G. Ciuti, M. Cianchetti and A. Menciassi, *IEEE/ASME Trans. Mech.*, 2017, **22**, 1881–1888.
11 C. Hegde, J. Su, J. M. R. Tan, K. He, X. Chen and S. Magdassi, *ACS Nano*, 2023, **17**, 15277–15307.
12 J. C. Yeo, H. K. Yap, W. Xi, Z. Wang, C. H. Yeow and C. T. Lim, *Adv. Mater. Technol.*, 2016, **1**, 1600018.
13 S. Din, W. Xu, L. K. Cheng and S. Dirven, *IEEE Sens. J.*, 2017, **17**, 5678–5686.
14 Y. Jin, S. a Xue and Y. He, *Adv. Mater.*, 2025, **37**, 2500076.
15 T.-W. Sun, M. Venkatesan, Y.-C. Hsu, J. Chandrasekar, W.-C. Chen, J.-S. Bénas, C.-J. Cho, J.-H. Lin, F.-C. Liang and A. Y. Rwei, *Nano Energy*, 2025, **133**, 110416.
16 A. Kumar, *Manuf. Lett.*, 2018, **15**, 122–125.
17 G. Liu, Q. Tan, H. Kou, L. Zhang, J. Wang, W. Lv, H. Dong and J. Xiong, *Sensors*, 2018, **18**, 1400.

18 G. A. Salvatore, J. Sülzle, F. Dalla Valle, G. Cantarella, F. Robotti, P. Jokic, S. Knobelspies, A. Daus, L. Büthe and L. Petti, *Adv. Funct. Mater.*, 2017, **27**, 1702390.
19 Q. Jiang, M. F. Antwi-Afari, S. Fadaie, H.-Y. Mi, S. Anwer and J. Liu, *Nano Energy*, 2024, **131**, 110252.
20 Y. Hou, L. Wang, R. Sun, Y. Zhang, M. Gu, Y. Zhu, Y. Tong, X. Liu, Z. Wang and J. Xia, *ACS Nano*, 2022, **16**, 8358–8369.
21 Q. Meng, W. Tian, W. Yin, D. Na, J. Zhu, S. He, S. Han and S. Peng, *ACS Appl. Polym. Mater.*, 2025, **7**, 13673–13684.
22 Z. Rao, F. Ershad, A. Almasri, L. Gonzalez, X. Wu and C. Yu, *Adv. Mater. Technol.*, 2020, **5**, 2000233.
23 W. Heng, S. Solomon and W. Gao, *Adv. Mater.*, 2022, **34**, 2107902.
24 X. Wang, Z. Liu and T. Zhang, *Small*, 2017, **13**, 1602790.
25 Y. Yin, C. Guo, H. Li, H. Yang, F. Xiong and D. Chen, *Sensors*, 2022, **22**, 5089.
26 E. Aslanidis, E. Skotadis and D. Tsoukalas, *Nanoscale*, 2021, **13**, 3263–3274.
27 Q. Yu, R. Ge, J. Wen, T. Du, J. Zhai, S. Liu, L. Wang and Y. Qin, *Nat. Commun.*, 2022, **13**, 778.
28 M. Amjadi, M. Turan, C. P. Clementson and M. Sitti, *ACS Appl. Mater. Interfaces*, 2016, **8**, 5618–5626.
29 Y. Yao, H. Dai, M. Ji, Y. Han, B. Jiang, C. Cheng, X. Song, Y. Song and G. Wu, *Electron. Mater. Lett.*, 2024, **20**, 684–693.
30 J. Chen, G. Zhu, F. Wang, Y. Xu, C. Wang, Y. Zhu and W. Jiang, *Compos. Sci. Technol.*, 2021, **213**, 108932.
31 S. Peng, S. Wu, Y. Yu, Z. Sha, G. Li, T. T. Hoang, M. T. Thai, T. N. Do, D. Chu and C. H. Wang, *J. Mater. Chem. A*, 2021, **9**, 26788–26799.
32 S. Peng, S. Wu, Y. Yu, P. Blanloeuil and C. H. Wang, *J. Mater. Chem. A*, 2020, **8**, 20531–20542.
33 T. Wang, Z. Qiu, H. Li, H. Lu, Y. Gu, S. Zhu, G. S. Liu and B. R. Yang, *Small*, 2023, **19**, 2304033.
34 Z. Sun, S. Yang, P. Zhao, J. Zhang, Y. Yang, X. Ye, X. Zhao, N. Cui, Y. Tong and Y. Liu, *ACS Appl. Mater. Interfaces*, 2020, **12**, 13287–13295.
35 J.-H. Lee, Y.-N. Kim, J. Lee, J. Jeon, J.-Y. Bae, J.-Y. Lee, K.-S. Kim, M. Chae, H. Park and J.-H. Kim, *Sci. Adv.*, 2024, **10**, eads9258.
36 Z. Yunlei, L. Haoxiang, L. Zhenlei, Y. Liting, J. Qian, L. Kan, Q. Fei and H. YongAn, *View*, 2022, **3**, 20220025.
37 Y. Zhang, H. Wu, L. Liu, Y. Yang, C. Zhang and J. A. Duan, *Polymers*, 2024, **16**, 2535.
38 X. Zeng, Y. Lu, L. Zou, Z. Pu, D. Chen, Z. Ding, Y. Fan, Y. Wang and Y. V. Li, *Chem. Eng. J.*, 2025, **510**, 161566.
39 X. Meng, T. Sun, L. Liu, C. Zhang, H. Zhao, D. Wang, J. Zhang, S. Niu, Z. Han and L. Ren, *ACS Appl. Mater. Interfaces*, 2022, **14**, 29441–29450.
40 Y. Guo, H. Guo, Y. Han, X. Chen, J. Liu, M. Yang, T. Lu, J. Luo, R. Tao and Q. Yang, *Adv. Funct. Mater.*, 2023, **33**, 2306820.
41 X. Wu, X. Luo, Z. Song, Y. Bai, B. Zhang and G. Zhang, *Adv. Funct. Mater.*, 2023, **33**, 2303504.
42 Q. Meng, T. Chi, S. Guo, M. Razbin, S. Wu, S. He, S. Han and S. Peng, *Mater. Horiz.*, 2025, **12**, 178–189.
43 I. Bozyel, Y. I. Keser and D. Gokcen, *Sens. Actuators, A*, 2021, **332**, 113056.
44 B. Zazoum, K. M. Batoo and M. A. A. Khan, *Sensors*, 2022, **22**, 4653.
45 L. Wu, J. Xue, J. Meng, B. Shi, W. Sun, E. Wang, M. Dong, X. Zheng, Y. Wu and Y. Li, *Adv. Funct. Mater.*, 2024, **34**, 2316712.
46 H. Wei, X. Li, F. Yao, X. Feng and X. Zhu, *Nanotechnol. Precis. Eng.*, 2024, 7.
47 W. Zhu, S. Wang, Y. Lu, W. Yang, S. Ge, Z. Lou, S. He, S. Jiang and J. Han, *Ind. Crops Prod.*, 2024, **222**, 119598.
48 X. Mou, Z. Yang, X. Lai, J. Ding, Y. Chen, H. Li and X. Zeng, *Chem. Eng. J.*, 2024, **493**, 152876.
49 E. Xie, Q. Xiao, W. Fan, H. Jamshaid, L. Guo and W. Wang, *ACS Omega*, 2025, **10**, 13218–13227.
50 X. Wang, M. Qu, K. Wu, D. W. Schubert and X. Liu, *Adv. Compos. Hybrid Mater.*, 2023, **6**, 63.
51 S. Han, S. Li, D. Liu, Y. Dong, Z. Gao, Y. Zhang and Q. Meng, *Polym. Compos.*, 2024, **45**, 9209–9223.
52 S. Han, S. Li, X. Song, Z. Zhou, Q. Meng, S. Araby and A. A. Abdelsalam, *Virtual Phys. Prototyping*, 2024, **19**, e2368644.
53 S. Han, S. Li, X. Zhang, D. Liu, S. Guo, B. Wang and Q. Meng, *Constr. Build. Mater.*, 2024, **435**, 136721.
54 H. Xu, W. Zheng, Y. Wang, D. Xu, N. Zhao, Y. Qin, Y. Yuan, Z. Fan, X. Nan and Q. Duan, *Nano Energy*, 2022, **99**, 107384.
55 O. A. Araromi, M. A. Graule, K. L. Dorsey, S. Castellanos, J. R. Foster, W.-H. Hsu, A. E. Passy, J. J. Vlassak, J. C. Weaver and C. J. Walsh, *Nature*, 2020, **587**, 219–224.
56 S. Lee, A. Reuveny, J. Reeder, S. Lee, H. Jin, Q. Liu, T. Yokota, T. Sekitani, T. Isoyama and Y. Abe, *Nat. Nanotechnol.*, 2016, **11**, 472–478.
57 S. Li, Y. Li, S. Han, G. Dong, K. Wang, Y. Dong and Q. Meng, *J. Ind. Eng. Chem.*, 2026, DOI: 10.1016/j.jiec.2026.01.005.
58 Q. Meng, Q. Liu, S. Li, Y. Li, K. Wang, L. Chen and S. Han, *Chem. Eng. J.*, 2025, 169416.
59 Q. Meng, S. Liu, Y. Yu, X. Gong, B. Wang, J. Ma and S. Han, *ACS Appl. Polym. Mater.*, 2026, **8**(4), 2815–2830.
60 X. Wang, H. Zhou, M. Chen, Y. He, Z. Zhang, J. Gan and Z. Yang, *Adv. Intell. Syst.*, 2023, **5**, 2200344.
61 S. Dong, Q. H. Feng and Y. B. Shi, *Sens. Actuators, A*, 2025, **395**, 117022.
62 W. Zhou, Y. Du, Y. Chen, C. Zhang, X. Ning, H. Xie, T. Wu, J. Hu and J. Qu, *Nano-Micro Lett.*, 2025, **17**, 68.